Size- and Temperature-Dependent Lattice Anisotropy and Structural Distortion in CsPbBr₃ Quantum Dots by Reciprocal Space X-ray Total Scattering Analysis

Federica Bertolotti, Nicola Dengo, Antonio Cervellino, Maryna I. Bodnarchuk, Caterina Bernasconi, Ihor Cherniukh, Yuliia Berezovska, Simon C. Boehme, Maksym V. Kovalenko, Norberto Masciocchi,* and Antonietta Guagliardi*

Lead halide perovskite nanocrystals (NCs) have emerged as next-generation semiconductors capable of unifying superior photoemission properties, facile and inexpensive preparation, compositional and structural versatility. Among them, CsPbBr₃ is a model system in theoretical and experimental studies owing to its intrinsic chemical stability. Nonetheless, knowledge of the precise magnitude and the size- and temperature-dependent lattice and structural distortions is lacking, and the static/dynamic nature of disorder in NCs remains an open question. Herein, robust reciprocal space X-ray total scattering analysis is applied and accurate lattice distortions, Pb—Br bond distances, and Pb—Br—Pb angles versus NCs size are extracted. The lattice anisotropy increases upon expansion on downsizing while, upon contraction on cooling, the lattice distortion behaves differently at intermediate (9 nm) and ultrasmall (5 nm) sizes and from the bulk. Bond distances (stretched by ≈1%) do not show any size dependence, whereas equatorial and axial angles denote more symmetric octahedral arrangements in the smallest sizes, where they differ by ≈2° compared to ≈8° in the bulk. Anomalously high atomic displacement parameters of axial bromine ions persisting down to cryogenic temperatures suggest statically disordered octahedral tilts. These results provide insights having important implications on size-dependent emission properties and the exciton fine structure.

1. Introduction

Colloidal lead halide perovskite (LHP) nanocrystals (NCs) are of great interest as novel light sources.[1–9] Their outstanding opto-electronic properties, facile and inexpensive preparation methods – over versatile compositions – and superior photo- or electrically-induced performances have impelled rapid incorporation of LHP NCs into displays and LEDs, and fostered novel applications as solution-grown light and quantum emitters or absorbers.[10,11] Over the past few years, great advances have concerned device optimization and quantum efficiencies,[1,12–15] fundamental studies (focusing on the effects of surface chemistry and NCs morphology on the light emissivity and long-term stability),[16] ab-initio calculations (elucidating the origin of LHP defect-tolerant electronic structure and providing the formation energy of defects and justification for their relative abundance),[17–28] and a blooming research on collective emissive states (through NC self-assembly into long-range ordered superlattices).[29–36] In all these studies,

F. Bertolotti, N. Dengo, N. Masciocchi
Dipartimento di Scienza e Alta Tecnologia & To.Sca.Lab
Università dell'Insubria
22100 Como, Italy
E-mail: norberto.masciocchi@uninsubria.it

A. Cervellino
Photon Science Division
Laboratory for Synchrotron Radiation - Condensed Matter
Paul Scherrer Institut
5232 Villigen, Switzerland

The ORCID identification number(s) for the author(s) of this article can be found under https://doi.org/10.1002/sstr.202300264.

M. I. Bodnarchuk, C. Bernasconi, I. Cherniukh, Y. Berezovska,
S. C. Boehme, M. V. Kovalenko
Institute of Inorganic Chemistry
Department of Chemistry and Applied Biosciences
ETH Zürich
CH-8093 Zürich, Switzerland

M. I. Bodnarchuk, C. Bernasconi, I. Cherniukh, Y. Berezovska,
S. C. Boehme, M. V. Kovalenko
Laboratory for Thin Films and Photovoltaics
Empa-Swiss Federal Laboratories for Materials Science and Technology
CH-8600 Dübendorf, Switzerland

A. Guagliardi
Istituto di Cristallografia & To.Sca.Lab
Consiglio Nazionale delle Ricerche
22100 Como, Italy
E-mail: antonella.guagliardi@ic.cnr.it

CsPbBr$_3$ NCs have acted as a model system for unveiling fundamental structure–function relationships,[37–41] similar to the extensive studies on CdSe-based NCs in the realm of II–VI compounds. LHP NCs differ vastly from classical colloidal quantum dots (QDs), foremost owing to the intrinsic lattice softness and dynamics as a major feature of LHP.[42–46] Besides the facile (isovalent) anion and cation substitutions (for X and A sites of the APbX$_3$ formulation),[47–54] favoured by the presence of point defects (vacancies) with low formation energy,[27] LHP NCs are prone to accommodate both larger lattice distortions and different types of structural (static and dynamic) disorders than classical QDs.[4] Nonetheless, only a limited number of studies focus on specific size-dependent structural effects in CH$_3$NH$_3$PbI$_3$ and CsPbI$_3$ NCs which are concurrent to quantum confinement but influence the energy bandgap and emission properties in a distinctive way.[42,55] In this regard, ab initio methods have elucidated both the effect of octahedral tilting (deviating from the straight configuration of the archetypical cubic polymorph) on widening the energy bandgap and that of lattice contraction on narrowing it.[56,57] Theory and experiments at a single NC level attribute the main emission of LHP NCs to the bright triplet exciton transition, with additional low-energy (weaker) spectral features detectable at cryogenic temperatures.[41,58] Size-dependent lattice anisotropy (consisting of tiny tetragonal and orthorhombic deviations from the cubic cell) is unveiled as an important mechanism governing the bright exciton fine structure splitting in CsPbI$_3$, which is an essential property (jointly to single-photon emission purity) for applying halide perovskite NCs in quantum information technology.[31,36,59–61] Concerning CsPbBr$_3$, the NC shape anisotropy is also reported to govern the excitonic fine structure.[62] On the side of structural disorder, the current debate on the existence of static disorder, possibly coexisting with a dynamic one, remains a non-trivial task to be solved in halide perovskites, both at bulk and nanoscale.[63–66]

Despite all these aspects playing a central role in the understanding of photoexcited phenomena and their timescale, a comprehensive quantitative picture of size-driven lattice and structural distortions based on experimental evidence in the model CsPbBr$_3$ NC system is lacking, and the (static and/or dynamic) nature of disorder remains an open question. This circumstance may be attributed to two major factors. Firstly, most of the structural studies on CsPbBr$_3$ QDs have been performed on cuboidal NCs of 9–12 nm in size. At these (and larger) sizes, there is wide consensus on that NCs exhibit (at room temperature) the thermodynamically stable orthorhombic phase, as observed in the bulk. The quite modest range of (until recently) available sizes, mainly due to the intrinsic instability of ultrasmall NCs (<7 nm), has hampered an in-depth quantitative investigation of size-dependent structural changes. These changes may refer to the possible stabilization of high(er) symmetry polymorphs (namely cubic, as claimed in many papers),[46,67–71] or to the onset of octahedral distortions as measured by the Pb—Br bond distances, Pb—Br—Pb bond angles and/or metal off-centering changes.[72,73] Lattice inflation is reported to occur in CsPbBr$_3$ NCs upon downsizing[74]; however no systematic study on its size dependence has ever been reported. Whether these effects are, fully or partially, governed by the NC size and/or surface passivation, and are measurable at all, has great

implications both on fundamental knowledge of LHP QDs and on the precise engineering and control of their function.[75–77]

The second factor thus far limiting a comprehensive picture of size-dependent structural effects is the inadequacy of conventional atomic-precise (namely, X-ray-based) structural methods of analysis in extracting robust quantitative information from experimental scattering data of NC ensembles, yet a highly challenging task at very small sizes. A more robust analysis comes within reach, thanks to the progress in wide angle X-ray total scattering (WAXTS) methods of characterization, particularly those developed in the reciprocal space (the so-called WAXTS-DSE - Debye scattering equation-based techniques).[78–80] The ultimate power of these techniques is the ability of DSE to treat on an equal basis Bragg and diffuse (elastic) scattering from the sample, which are simultaneously collected through a WAXTS experiment (details in Supporting Information). Remarkably, the diffuse scattering significantly contributes to the total pattern in small NCs, as it results from finite-size effects, defects and disorder (i.e., from any deviation from an average long-range periodic order), but it is fully disregarded in conventional diffraction methods. The DSE-based analysis of WAXTS data relies on atomistic models of NCs of well-defined size and shape, and therefore encodes all relevant atomic and nanometre length scales within a unified and reliable physical model. Specifically, in the field of ultrasmall semiconductor colloidal QDs, WAXTS-DSE methods have been successfully applied in many different cases,[81,82] including unveiling planar defects of the twin boundaries type in CsPbBr$_3$ NCs[74] and local low-symmetry arrangement in cubic hybrid halide perovskite NCs (FAPbBr$_3$, FA = CH(NH$_2$)$_2$$^+$).[48,83,84]

In the present work, we present a thorough analysis of colloidal CsPbBr$_3$ NCs with sizes in the 5–20 nm range. Based on synchrotron WAXTS data, herein we apply the DSE method of analysis by constructing atomistic models of cuboidal NCs and calculating the X-ray pattern model of the ensemble (see Supporting Information). We further combine this approach with an optimization procedure against experimental data exploring the model parameters hyperspace, to limit and control correlation effects. The analysis is performed on both WAXTS data collected directly on colloidal suspensions of CsPbBr$_3$ NCs, at room temperature, and on variable-temperature data measured on dry samples, from 300 K down to 6 K, for intermediate and small sizes. We extract lattice anisotropy, bond distances, and angles and discuss their size- and temperature-dependence, while also accounting for the structural inequalities of equatorial (Br$_{eq}$) and axial (Br$_{ax}$) bromines within the orthorhombic structure. At room temperature, below 7 nm (the size at which NCs also enter the strong quantum confinement regime), the equatorial Pb—Br—Pb bending nearly equals the axial one, thus exhibiting a significant deviation from the bulk (where the two angles differ by ≈8°) in favour of a more symmetric arrangement (in spite of the large orthorhombic strain). Upon cooling, we find that the lattice distortions in 9 nm and 5 nm NCs are dissimilar. Finally, we provide evidence of the existence of a static disorder of PbBr$_6$ octahedral tilting, particularly evident in the axial direction, likely coexisting with the dynamic disorder of halides. Implications of these findings on the reported emission properties are also briefly discussed.

**ADVANCED
SCIENCE NEWS**

www.advancedsciencenews.com

**small
structures**

www.small-structures.com

2. Results

2.1. Size-Driven Lattice Response and Parameters Accuracy at Ultrasmall Sizes

The CsPbBr$_3$ NCs selected for this study cover the 5–20 nm size range and have been prepared mostly according to the synthesis in ref. [5] or modifications thereof.[18] Though not critical for the scope of the present work, our strategy of size selection (within the range of interest) considers slightly different synthetic

approaches and/or capping ligands (oleic acid/oleylammonium – OAc/OAm, didodecyldimethyl ammonium bromide – DDAB, oleylguanidinium bromide – OGB, and others, see Experimental Section). This choice guarantees access to stable colloidal NCs with high uniformity in size and shape for each representative size (TEM images in **Figure 1**a and S1, Supporting Information). On the other side, in spite of being a key factor for the NC quantum efficiency, only a minor influence of surface chemistry over the investigated structural properties is observed, in line with reported calculations and experimental work on this specific
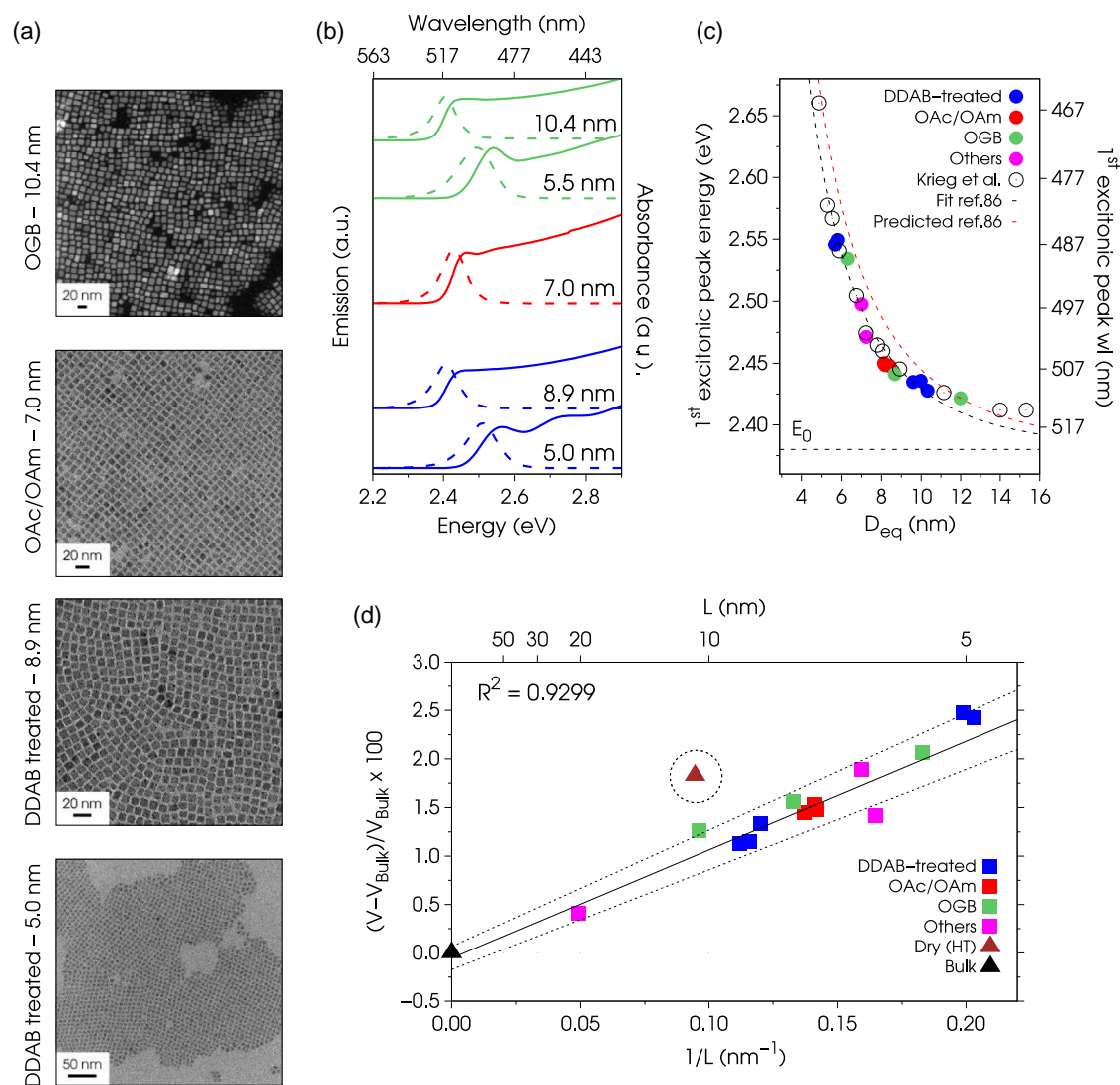

Figure 1. Size-dependent (room-temperature) properties of colloidal CsPbBr$_3$ NCs synthesized with different passivation methods. a) TEM images (scale bars 20 nm or 50 nm) and b) absorption and photoluminescence spectra of representative NCs sizes (edge length L) and surface ligands (see colours legend in panel d). c) Energy of the first exciton peak vs NCs sizes (defined as equivalent diameter of a sphere, $D_{eq} = 2L/\sqrt{3}$). The fitting (black dashed) and predicted (red dashed) curves are described by the semi-empirical equation of optical band gaps vs sizes, as suggested in ref. [85], with $E_0 = 2.38$ eV the reference bulk value (details in the Experimental Section). The empty white circles from ref.[33] (prepared using zwitterionic ligands, sizes from SAXS analysis) nicely follow the curve and further support the hypothesis of a limited influence of the surface chemistry. Worth to note, the 5.0 nm spectrum in (b), exhibits a second broad peak ($\approx$2.7 eV) originating from the allowed p–p excitonic transition, as reported in ref. [33] d) Relative volumetric lattice strain vs L over the 5–20 nm size range. V is the volume of the *Pbnm* unit cell of NCs, V_{Bulk} (black triangle) is that of the bulk from ref. [92]. The solid black line is the regression line best fitting all points, the dotted lines depend on the estimated standard deviation of the line coefficients. Values of V and L are extracted from X-ray analysis of data collected on colloidal NCs. The circled brown triangle outlier refers to the volume extracted from X-ray data collected at 410 K on the 10 nm NCs dried sample.

**ADVANCED
SCIENCE NEWS**

www.advancedsciencenews.com

**small
structures**

www.small-structures.com

aspect.[24] A minor influence of the surface chemistry (as compared to the influence of NC size) is also observed in the absorption and emission spectra of all samples, as shown in Figure 1b and S1, Supporting Information, for cuboidal NCs with several edge lengths L, extracted from WAXTS-DSE analysis (see Table S1, Supporting Information). Irrespective of the employed ligands, the first exciton peak position (obtained by a second-derivative approach[33]) of all NCs studied in this work nicely obeys a common size-dependent law (Figure 1c).[85] Nonetheless, to further support such a statement, and as done in Figure 1, in the following we maintain full track of the different surface chemistry by marking NCs from each group with the same colour code (for a total of 14 samples in four different groups).

To rationalize the size-dependent band gap in Figure 1c, we test our experimental data against the semi-empirical sizing function recently proposed in ref. [85] (details in the Experimental Section). This function predicts the size-dependent optical band gap of spherical semiconductor QDs using known bulk (i.e., size-independent) material parameters and considering a correction for non-parabolic energy bands. For our $CsPbBr_3$ QDs, the prediction (red dashed curve in Figure 1c) is obtained by considering the effect of the cuboidal NC shape on the energy confinement (via introducing an equivalent diameter $D_{eq} = 2L/\sqrt{3}$) and by assuming the following bulk parameters: optical band gap $E_0 = 2.38$ eV,[86] Bohr diameter of 6.1 nm and (high-frequency) dielectric constant $\varepsilon_\infty = 7.3$.[85,87] While using these reported bulk parameters already yields coarse agreement between experimental data and semi-empirical sizing function, we now further refine the latter via fitting. In principle, deviations from the bulk $CsPbBr_3$ crystal structure in NCs (vide infra) could impact each of the three employed "bulk" material parameters. However, for simplicity, we here choose to fix the bulk gap and dielectric constant at the reported bulk values while treating the Bohr diameter as a free fit parameter in our NCs. This yields an improved fit (black dashed curve in Figure 1c) to the experimental data (including the data from ref. [33]), with a Bohr diameter of 5.05(8) nm, slightly reduced compared to the reported bulk value. A detailed study of size-dependent optical properties is beyond the scope of our present work.

Nonetheless, we here suggest that deviations from the simple size confinement as given in ref.[85] would not be unsurprising if the crystal structure itself is size-dependent (vide infra). Finally, we suggest that the size dependence in Figure 1c offers itself a starting point for such further studies, given the high accuracy of our NC size determination via utilizing two independently collected datasets (WAXTS, this work, and small angle X-ray scattering, (SAXS), ref. [33]).[85,88]

In this regard, herein atomistic models of $CsPbBr_3$ NCs are built using the orthorhombic crystal structure (in the *Pbnm* setting)[74,89,90] and a cuboidal (orthogonal square prisms) morphology, with morphological axes running parallel to the crystallographic ones (details in the Supporting Information). Four parameters of size (more appropriate for the prismatic NCs) are adjusted according to a bivariate distribution function (average size and standard deviation along the crystallographic c axis – L_c – and in the orthogonal ab plane - L_{ab}, the two treated as independent directions, details can be found in ref. [91]). From

these values (reported in Table S1, Supporting Information), $L = (L_c L_{ab}^2)^{1/3}$ is extracted as a single measure of the NC average cube edge length. The bivariate model of size indeed provides quite isometric lengths for the different samples (the average aspect ratio L_c/L_{ab} is 1.14 with standard deviation 0.14, with no clear size-dependence), suggesting that L is a good proxy for the NC size (at least for the scope of the present work).

In Figure 1d we show the lattice expansion resulting from the X-ray analysis versus $1/L$. We plot the relative deviation of the unit cell volume V (see Table S2, Supporting Information) from that of the bulk material (V_{Bulk}, as reported in ref. [92]) and notice a substantial alignment of all samples to the regression line ($R^2 = 0.9299$). Though quite modest at 20 nm ($\approx 0.4\%$), the lattice expansion sets the remarkable maximum volumetric strain of 2.3% at the smallest 5 nm size. The negative surface energy $\gamma = -2.7$ eV nm^{-2} (details in Supporting Information) extracted therefrom is in good agreement with the reported value of -3.0 eV nm^{-2} for OAc/OAm-capped $CsPbI_3$ NCs.[42] All points in Figure 1d refer to NCs in their colloidal state, except for the sample labelled as Dry (HT), for which the lattice expansion (1.9%) is measured on 10 nm NCs at 410 K, that is beyond the reported transition temperature to the cubic polymorph.[74,93] This value clearly indicates that the size-driven expansion observed in 5 nm NCs exceeds the thermally induced expansion in NCs of twice the edge length.

Inspired by this finding, we investigate in depth those structural effects possibly driven by such ultra-expansion of the lattice or, in other words, the possible stabilization of the cubic polymorph at room temperature.[46,67–71] Initially, the occurrence at 5 nm of the *Pm-3m* cubic structure (**Figure 2**a) vs the *Pbnm* orthorhombic one (Figure 2b) is tested and a clear indication in favour of the latter is measured by the much lower Goodness of Fit statistical figure of merit, GoF (2.44 vs 1.57, respectively). We further test a split-cubic model encoding the structural configuration that combines a lower-symmetry local atomic arrangement (octahedral tilting) within an average cubic structure (Figure S2, Supporting Information), which is supported by the recent literature on both fully inorganic and organic–inorganic LHP NCs, and by ab initio calculations.[83,94–96] Despite the significant improvement of the latter model (GoF = 1.84) vs the unsplit *Pm-3m* one, the orthorhombic structure is still a far better match, suggesting that $PbBr_6$ octahedral tilting is coherent throughout most of the NC volume. Once this aspect has been clarified, aiming at achieving an in-depth atomic-precise comprehension of the size-dependence of $CsPbBr_3$ NC structural properties, we discuss in this section and in Section 2.2 the deviations of the orthorhombic lattice parameters from the cubic symmetry, in the ultra-expanded 5 nm NCs and larger sizes, whereas octahedral tilt variations in comparison to the unrelaxed structure of the bulk are treated in paragraph 2.3.

The a and b unit cell parameters in the orthorhombic halide perovskite structure are very similar and slightly differ from the a_k cubic lattice parameter according to the $a \approx b \approx \sqrt{2}a_k$ relationship (schematized in Figure 2c). As consequence, a and b are at risk of being easily interchanged when extracted from X-ray diffraction data possessing broad peaks, such as those of ultrasmall NCs (<7 nm). In such circumstances, determining
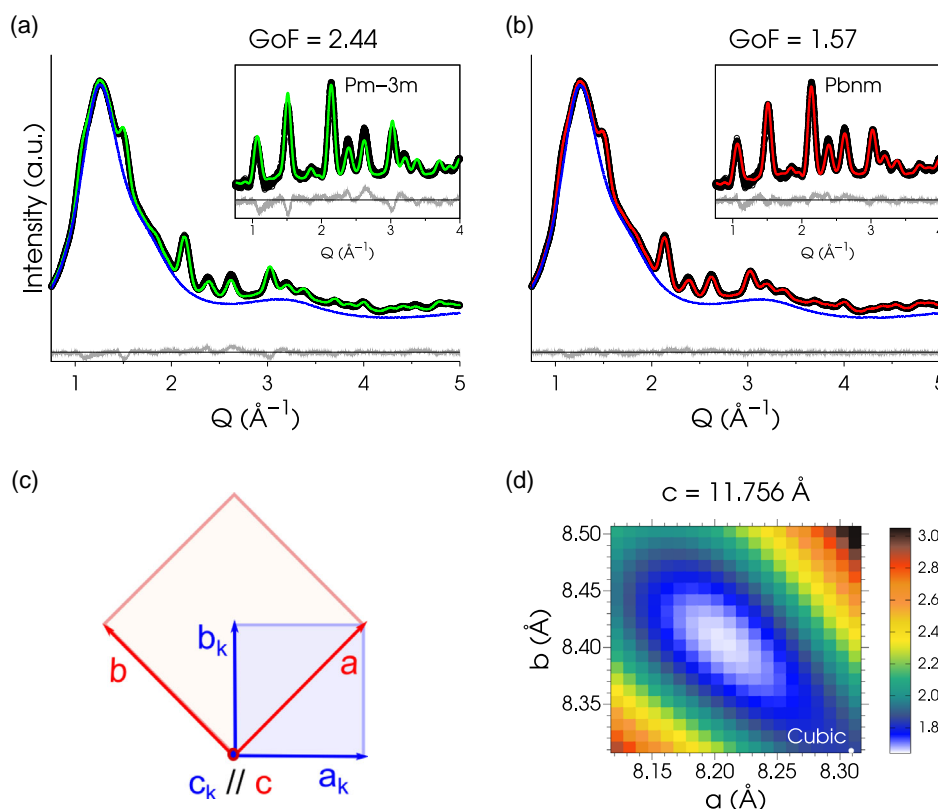
ADVANCED
SCIENCE NEWS
www.advancedsciencenews.com

small
structures

www.small-structures.com

Figure 2. WAXTS-DSE (room-temperature) crystal structure analysis of ultrasmall colloidal 5 nm CsPbBr$_3$ NCs. Best fit using a) the cubic *Pm-3m* and b) the orthorhombic *Pbnm* crystal structure models: experimental data (black dots), DSE pattern model (green and red traces), toluene (blue trace), residual (grey trace). c) Geometrical relationship between the orthorhombic (**a**, **b**, **c**) and cubic (**a**$_k$, **b**$_k$, **c**$_k$) unit cell vectors of LHP in the **ab**-plane; The **c** and **c**$_k$ axes, drawn out of the page, are parallel. d) 2D map of GoF (in colour-grade) vs orthorhombic *a* and *b* lattice parameters (at *c* = 11.756 Å). The minimum *GoF* is found at *a* = 8.207(1) Å and *b* = 8.407(1) Å (*a/b* = 0.976). The refined cell parameter of the *Pm-3m* model ($a_k = 5.875$ Å $= \frac{8.308}{\sqrt{2}}$ Å) is highlighted by the white spot in the map (bottom-right corner). For the estimation of uncertainties, details are given in the Supporting Information.

robust values (by well-established optimization algorithms implemented in Rietveld-based software programs) is quite challenging. Herein, we apply a more robust approach of parameter hyperspace exploration through a fine grid-search (grid step = 0.01 Å), carried out while fixing all other structural and morphological model parameters to pre-refined values, and measuring the match of each grid point model to the experimental data using the GoF indicator, as shown in Figure 2d for the 5 nm NCs. The 3D map of GoF vs *a* and *b* lattice parameters, at (optimized) *c* = 11.756(2) Å, locates the minimum GoF at *a* = 8.207(1) Å and *b* = 8.407(1) Å. Though the shape of the GoF basin indicates a clear anticorrelation of the *a* and *b* parameters, the minimum is evidently distinct from the cubic value of the *Pm-3m* and split-cubic models (the white dot in the bottom-right corner in Figure 2c, where $a_k = 8.308/\sqrt{2}$ Å = 5.875 Å), despite the apparently small, but measurable, deviation of *a* and *b* (0.2 Å).

2.2. Size- and Temperature-Dependent Lattice Anisotropy

The size-driven (room-temperature) variation of unit cell parameters over the 5–11 nm range of sizes is shown in **Figure 3**a. The

a parameter is found to be rather insensitive to the NC size, which mostly affects *b* and *c* values, the former exhibiting a more pronounced size dependence. To better understand the meaning of this finding in terms of distortion of the orthorhombic lattice vs the cubic one, we refer to the theory presented in ref. [62] and plot in Figure 3b the irreducible orthorhombic strain ζ vs *L*. ζ quantifies the strain along the *a*, *b*, *c* orthorhombic axes relative to a pseudo-cubic structure. This is described as a non-primitive supercell with axes parallel to the orthorhombic ones and lengths $a_C = \sqrt{2}a_k$, $b_C = \sqrt{2}a_k$, and $c_C = 2a_k$, where $a_k = \sqrt[3]{(abc)/4}$ is the equivalent lattice parameter of the primitive cubic cell. Based on this relation, strain components [$\varepsilon_{aa} = (a - \sqrt{2}a_k)/\sqrt{2}a_k$ and $\varepsilon_{bb} = (b - \sqrt{2}a_k)/\sqrt{2}a_k$] are calculated from the X-ray-based results, from which $\zeta = (\varepsilon_{aa} - \varepsilon_{bb})/2$ is obtained. The higher the $|\zeta|$ values, the more distorted the lattice.

Figure 3b indicates that, compared to the rather modest value of the reference bulk, CsPbBr$_3$ NCs exhibit higher orthorhombic strain that systematically increases upon downsizing, that is while their cell volume expands (Table S2, Supporting Information). A similar size dependence of the lattice anisotropy is reported in CsPbI$_3$ NCs[42] where it is indicated as the major mechanism inducing bright-exciton fine structure splitting
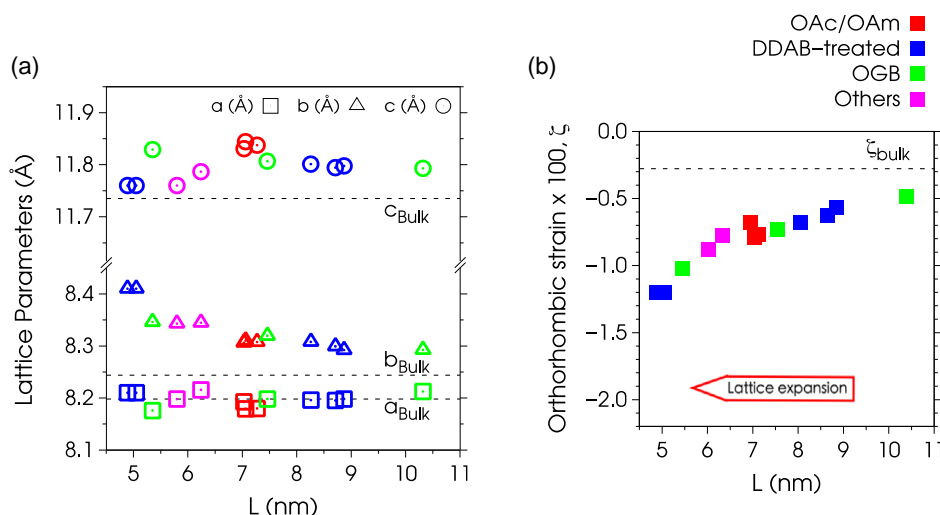
Figure 3. a) Room-temperature lattice parameters and b) lattice strain of CsPbBr$_3$ NCs vs size (X-ray data from colloidal suspensions): a) Orthorhombic *a* (squares), *b* (triangles) and *c* (circles) parameters vs edge length *L* of cuboidal NCs; b) Irreducible orthorhombic strain ζ vs *L*. ζ describes the lattice anisotropy measured as deviations from the axes of a non-primitive pseudo-cubic cell, as described in the main text. The strain increases with lattice expansion upon downsizing.

(at the ensemble level) at low temperature in solution-grown QDs. This effect is deemed important for highly coherent single-photon emission and application of perovskite NCs in quantum information technology.[60] This is a hot topic in the field of LHP QDs, as demonstrated by the flourishing number of reports on low-T spectroscopic experiments and related fundamental works.[38,41,97–101]

Indeed, the NC response to cooling was shown to increase the lattice anisotropy of CsPbI$_3$ NCs. To check whether such a hypothesis is valid also for CsPbBr$_3$ NCs, we further performed variable-*T* measurements, from 300 K down to 6 K, on dried NCs for the 5 nm and 9 nm didodecyldimethyl ammonium bromide (DDAB)-capped samples (see Experimental Section). **Figure 4**a shows the progressive lattice contraction, given as the unit cell volume of the equivalent primitive cubic cell ($V_{cubic} = V_{ortho}/4$), indicating that the NC volumetric response is size-independent, with a common thermal expansion coefficient ($\alpha_V = 1.1 \times 10^{-4}$ K^{-1}) derived therefrom (see Supporting Information) very close to the reported bulk value.[92] The constant offset between the 5 nm and 9 nm curves in Figure 4a depends on the different lattice expansion already found at room temperature (2.3% vs bulk for 5 nm and 1.1% for 9 nm), to which the metrical differences detected at different *T* can be reasonably attributed. In this regard, the *T*-dependence of ζ exhibited by the 9 nm NCs in Figure 4b is in line with the trend reported in CsPbI$_3$ NCs. In contrast, at the ultrasmall 5 nm NC size, such dependence nearly vanishes, leading, at cryogenic temperatures, to a less distorted lattice than for the 9 nm NCs. By adding in Figure 4b the ζ values of the bulk at 300, 100, and 4 K (calculated from ref. [102]), it becomes clear that the slope of the strain decreases from the bulk to the 9 nm to the 5 nm NCs. This behaviour originates from the *a*, *b*, *c* parameters (different in the two NC sizes and in the bulk) at room temperature and their distinctive dependence on *T* (Figure 4c). For bulk/large NCs (exhibiting higher order at low *T*) this can be seen as an increase of

disordering (higher entropy/higher symmetry) upon heating. We finally remark that ζ increases with *L* (becoming less negative, Figure 3b) while the NCs lattice contracts, and increases with *T* (Figure 4b) while the NC lattice expands (i.e., the slopes of $\zeta \geq 0$ in both cases).

2.3. Determining Pb—Br Bond Distances and Pb—Br—Pb Bond Angles via Grid-Search χ^2-Minimization

In this section we discuss the method for extracting robust Pb—Br bond distances and PbBr$_6$ octahedral tilts from WAXTS data collected on the NC colloidal suspensions. We exemplify the method in **Figure 5** for the 5 nm NCs; calculations for all NC sizes are available in Figure S3–S6, Supporting Information. The method of investigation relies on a grid-search exploration of the (x,y,z) fractional coordinates of bromine atoms (bridging Pb atoms of corner-sharing octahedra, see Figure 5a) inside the orthorhombic unit cell, in the vicinity of their locations in the bulk.[92] We consider separately the equatorial (Br$_{eq}$) and axial (Br$_{ax}$) bromine atoms (structurally inequivalent) and use the Pb—Br$_{eq}$—Pb and Pb—Br$_{ax}$—Pb bond angles as proxies of the actual octahedral tilts.[103] The exploration is performed at fixed Pb and Cs positions (see Table S3, Supporting Information) and fixed values of the isotropic atomic displacement parameters – in the form of Debye–Waller (DW) factor (in the 1.0–6.0 Å^2 range, at 0.5 Å^2 steps). In this regard, intrinsic limitations of X-ray-based powder diffraction techniques, typically leading to poorly determined DW factors, jointly to the lack of computational tools implementing more complex atomic motions within the DSE method of analysis, dictates the choice of isotropic atomic displacement parameters (within the harmonic approximation of thermal motions). Such a choice does not significantly affect the major results of the structural analysis (as briefly discussed in Section 2.5), despite that anisotropic and anharmonic vibrations of halides in the LHP are supported by theoretical models
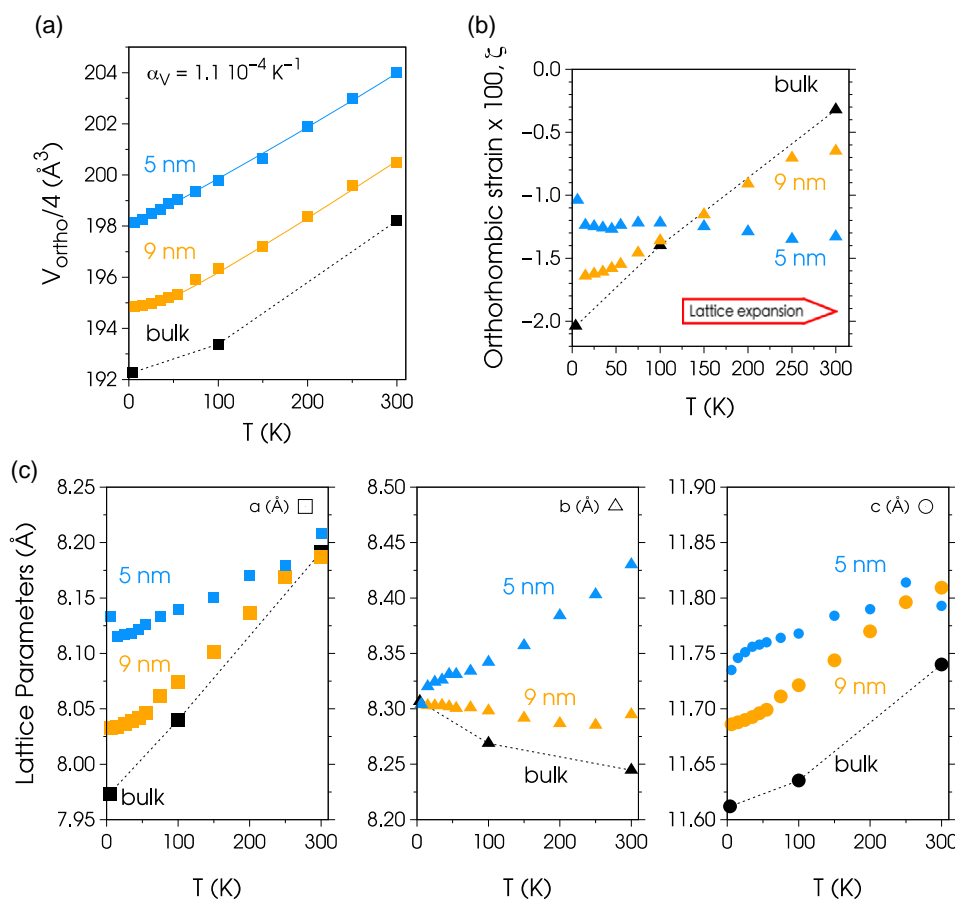
ADVANCED
SCIENCE NEWS
www.advancedsciencenews.com

small
structures
www.small-structures.com

Figure 4. a) Temperature-dependent unit cell volume, b) orthorhombic lattice strain ζ, and c) a, b, c cell parameters vs T of dried 9 nm (yellow symbols) and 5 nm (blue symbols) CsPbBr$_3$ NCs. Black symbols are bulk values at 300, 100 and 4 K, from ref. [102]. In (a), the unit cell volume is normalized to the cubic one. An equal volumetric thermal expansion coefficient is extracted therefrom. In (b) tiny differences from ζ values in Figure 3b at the same NC sizes are due to the sample drying. The slope of strain on cooling (upon lattice contraction) is size-dependent and decreases from bulk to the 9 nm to the 5 nm NCs.

and experimental evidence at the bulk scale, and their role in the photoexcited ultrafast dynamic response of halide perovskites is well recognized.[63–66,104–112]

Figure 5b shows the 3D maps of GoF $= (\chi^2)^{\frac{1}{2}}$ vs (x,y) for Br$_{eq}$ at $z = 0.486$ and at selected DW's, while maps for Br$_{ax}$ (at $z = 0.75$, symmetry-restrained) are displayed in Figure 5c. On one side, based on the grid exploration, Br's locations are pinpointed from the best match with the WAXTS data and Pb—Br distances and Pb—Br—Pb bond angles, derived therefrom, discussed vs the bulk angles and distances.[92] From the analysis of Br$_{eq}$ location in Figure 5b at its minimum GoF (found at DW $= 2.0$ Å^2), the resulting equatorial bending of 161.0(1)° is $\approx 4°$ off the bulk value of 157.42(6)°, whereas the two bond distances [Pb$_1$—Br$_{eq} = d_1 = 2.983(2)$ Å and Pb$_2$—Br$_{eq} = d_2 = 2.973(2)$ Å, see Figure 5d] are comparable and only slightly expanded vs the bulk distances [$d_1 \approx d_2 = 2.964(1)$ Å]. In a parallel way, the analysis of Br$_{ax}$ in Figure 5c (minimum GoF at DW $= 3.0$ Å^2), provides the axial bending of 163.2(2)° and distances Pb$_1$—Br$_{ax} = $ Pb$_3$—Br$_{ax} = d = 2.9710(8)$Å vs 165.5(1)° and 2.9575(5) of the bulk. On the other side, to evaluate how robust these results are, we further discuss the basins of competitive GoF's around the minima in Figure 5b,c (taken as representative of the

potential energy surface and curvature, details in the Supporting Information). These basins exhibit peculiar shapes that are maintained throughout the whole sequence of DW-maps. These features are replicated in all investigated sizes (see Figure S3–S6, Supporting Information), suggesting more general considerations regarding the size-driven changes of bond distances and PbBr$_6$ tilting.

To simplify the discussion, we schematize in Figure 5d,e the set of those positions (or movements) of Br$_{eq}$ matching the experimental observations. Positions in Figure 5d preserve nearly identical Pb—Br$_{eq}$—Pb angles (perfectly equal along the arc in Figure 5d) while d_1 and d_2 bond distances vary in a fully anticorrelated manner. Positions in Figure 5e exemplify the case of Br$_{eq}$ progressively changing the bond angle while preserving equal bond distances ($d_1 = d_2$). The trajectory in Figure 5d corresponds to positions along the AB dashed line in the experimental map of Figure 5b, whereas the trajectory in Figure 5e refers to positions along CD, nearly perpendicular to the AB path. Accordingly, the GoF variation along the AB path is plotted vs Pb—Br$_{eq}$ bond distances (the bending being essentially invariant), as displayed in Figure 5h. Here, the minimum GoF is found at $d_1 \approx d_2$ indicating that Br$_{eq}$ equidistant from Pb$_1$ and Pb$_2$ is the best

**ADVANCED
SCIENCE NEWS**

www.advancedsciencenews.com

**small
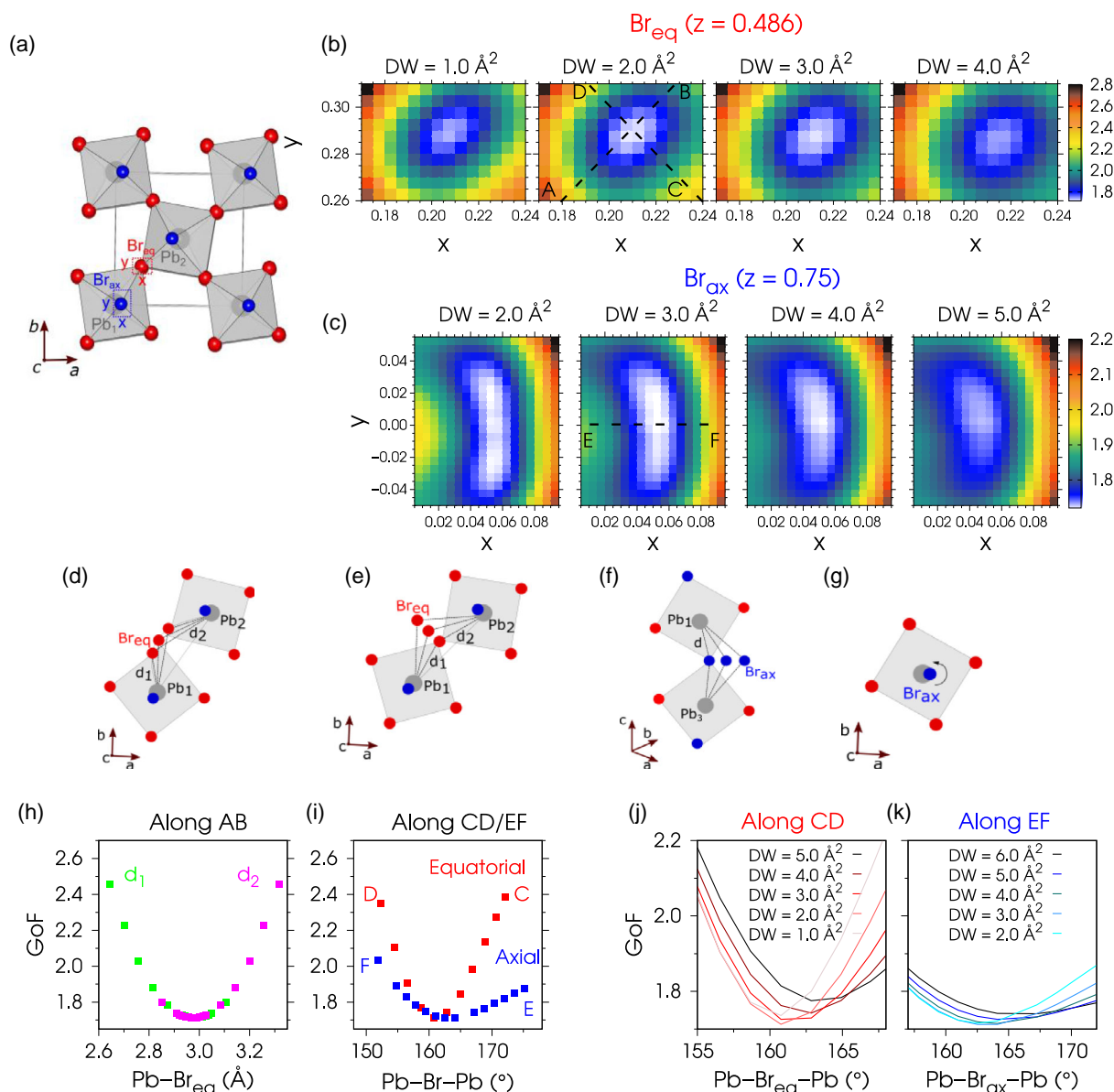structures**

www.small-structures.com

Figure 5. Grid-search exploration of Br_{eq} and Br_{ax} crystal coordinates and the resulting Pb—Br bond distances and Pb—Br—Pb bond angles for the 5 nm NCs. a) Schematics of the orthorhombic $CsPbBr_3$ crystal structure view down the *c*-axis: Br_{eq} (red), Br_{ax} (blue), Pb (grey), Cs atoms removed for the sake of clarity. The dotted rectangles exemplify the regions of exploration for Br_{eq} (red, bridging Pb_1 and Pb_2) and Br_{ax} (blue). b,c) 3D maps of GoF (in colour-scale) vs *x* and *y* fractional coordinates of b) Br_{eq} and c) of Br_{ax} at the DW value reported on top of each map. Maps are shown at the optimized $z = 0.486$ coordinate for Br_{eq} and at the symmetry-restricted $z = 0.75$ for Br_{ax}. The grid step of calculation is 0.001 (≈ 0.008 Å along *x* and *y*), re-binned at 0.005 (for sake of clarity). d,e) Schematics of the Br_{eq} trajectories along with the equatorial bending variations: d) bending remains nearly constant while Pb—Br_{eq} bond distances (d_1 and d_2) vary in a fully anticorrelated manner, e) bending varies while $d_1 = d_2$. Trajectories in (d) and (e) reproduce the AB and CD dashed lines in panel (b). f,g) Schematics of the Br_{ax} moves: f) in radial direction (off the *c*-axis) determining narrowing of the axial bending and concurrent increase of the Pb—Br_{ax} bond distance *d*, as per the moves along the EF dashed line in (c), and g) as apparent libration hinged on the *c*-axis reproducing the arc-shaped GoF basin observed in the maps in (c). GoF variations: h) along AB vs distances (Pb_1—$Br_{eq} = d_1$, green dots, and Pb_2—$Br_{eq} = d_2$, purple dots); i) along CD and EF vs angles (Pb—Br_{eq}—Pb, red, and Pb—Br_{ax}—Pb, blue), providing the best equatorial/axial angle, respectively; j) along CD at increasing DW of Br_{eq}, and k) along EF at increasing DW of Br_{ax}, showing concurrent small shifts towards higher equatorial and axial angles.

configuration for the 5 nm NCs. In a parallel way, the GoF variation along the CD path, plotted vs the equatorial bending in Figure 5i, leads to the best angle of 161°.

With reference to Br_{ax}, the peculiar arc-shaped basins of competitive GoF's in the maps of Figure 5c indicate that the atom

apparently librates about the *c*-axis and maintains nearly fixed bond distance and angle along the arc (see Figure 5g). The GoF basin shifts along the radial EF direction and gradually approaches the *c*-axis when the DW factor is raised, which causes the concurrent widening of the bond angle (as schematized in

Figure 5f). These observations point to a strong numerical correlation between the Br_{ax} position and its thermal displacement parameter. Such an effect is also noticeable, to a minor extent, for Br_{eq} in Figure 5b. The GoF variation along the EF path vs the $Pb—Br_{ax}—Pb$ angle (Figure 5i) further highlights the shallower profile for Br_{ax} than that of Br_{eq}. When CD/EF curves are extracted from the maps at increasing DW's, both equatorial (Figure 5j) and axial (Figure 5k) angles are slightly shifted toward higher values (by 3° at most), as per the correlation between Br location and thermal motion. While raising the GoF's, larger DW's do not significantly change the shallowness of profiles, a circumstance leading to a less accurate determination of the location of the axial vs the equatorial bromine, as discussed in the next section.

2.4. Size Effects on Pb—Br Bond Distances and Equatorial/Axial Pb—Br—Pb Bond Angles

The much shallower minimum of the $Pb—Br_{ax}—Pb$ curves is size-insensitive and is systematically detected in all samples. Indeed, it has a structural origin. We elucidate this effect in **Figure 6**a by showing for the 9 nm NCs the residual $(I–I_0)/I_0$ patterns, where I is calculated at different $Pb—Br_{eq}—Pb$ (from 160° to 166°) and fixed $Pb—Br_{ax}—Pb$ (158°) angles, (and vice versa) and I_0 is obtained by imposing equal equatorial and axial bending (158°). By varying the equatorial angle, the X-ray pattern intensity variations are much stronger than for an axial bending of equal extent, due to the presence of $Br_{eq}:Br_{ax}$ atoms in a 2:1 ratio in the orthorhombic space group. This intrinsically lower contribution to the scattering for Br_{ax} makes its position and the related structural properties less accurately determined than those of the equatorial bromine (by WAXTS-DSE and any type of diffraction-based analysis).

The correlation between Br atom position and thermal motion further complicates the task of achieving a robust structural

analysis for Br_{ax}. 3D maps of GoF's vs $Pb—Br_{eq}—Pb$ or $Pb—Br_{ax}—Pb$ angles and vs DW factors are assembled in Figure 6b for the 5 nm and 9 nm NCs by combining the GoF curves (shown in Figure 5j, k) calculated for the entire sequence of the DW-maps. Two major findings are highlighted: 1) the 9 nm NCs exhibit bond angles close to the bulk values, whereas the 5 nm NCs exhibit measurable differences from the 9 nm NCs regarding both the equatorial (by 4°) and axial (by 3°) angles; 2) the strong correlation between Br_{ax} position and its thermal displacement parameter is particularly severe at 5 nm but it is detected also at 9 nm and larger sizes, which points to an intrinsic structural disorder of Br_{ax} in $CsPbBr_3$ NCs (the nature of which is discussed in paragraph 2.5, based on variable-temperature data analysis).

A complete overview of Pb—Br bond distances and Pb—Br—Pb bond angles over the full range of sizes is provided in **Figure 7** (see Table S3 and S4, Supporting Information, best fit in Figure S7, Supporting Information). $Pb—Br_{eq}$ and $Pb—Br_{ax}$ distances vs L (Figure 7a) indicate systematic elongation vs bulk values, never exceeding ≈1%, without any clear evidence of a size-dependence. In contrast, the $Pb—Br_{eq}—Pb$ and $Pb—Br_{ax}—Pb$ angles vs L (Figure 7b) suggest that nanosizing down to 7 nm does not significantly affect octahedral reorientation, both as equatorial and axial tilts, whereas at smaller sizes the largest lattice expansion drives measurable changes of both angles, making bending softer than stretching. The changes of equatorial and axial bending take place in the opposite directions (at most, by ≈+4° and ≈–2° vs the bulk, respectively), eventually resulting in nearly comparable bond angles. This structural rearrangement is substantial, and it is expected to impact the $CsPbBr_3$ NCs photophysical properties (that strongly depend on octahedral tilting) concurrently to quantum confinement effects, but in a distinctive way.[55]

Summarizing, the high flexibility of $CsPbBr_3$ points to a peculiar, so far undetected, size-driven response upon NC downsizing towards nearly equal octahedral tilts in the *ab*-plane and normal
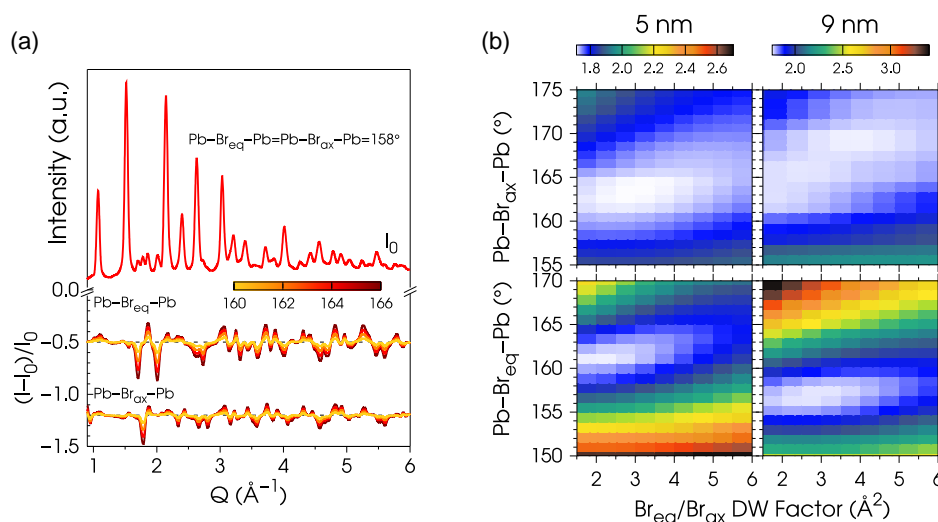

Figure 6. a) Simulated differential patterns $(I–I_0)/I_0$ for 9 nm $CsPbBr_3$ NCs that exemplify the progressive changes upon increasing equatorial $Pb—Br_{eq}—Pb$ bending (from 160° to 166°) at fixed axial angle $Pb—Br_{ax}—Pb = 158°$, and vice versa. The I_0 reference pattern is calculated at equal equatorial and axial angles (158°). b) 3D maps of GoF's (from the experimental grid coordinates exploration) vs equatorial/axial bending and vs Br_{eq} and Br_{ax} DW factors for the 5nm and 9 nm NCs. The two sizes exhibit equatorial angles differing by 4°, while axial angle differ by 3°.
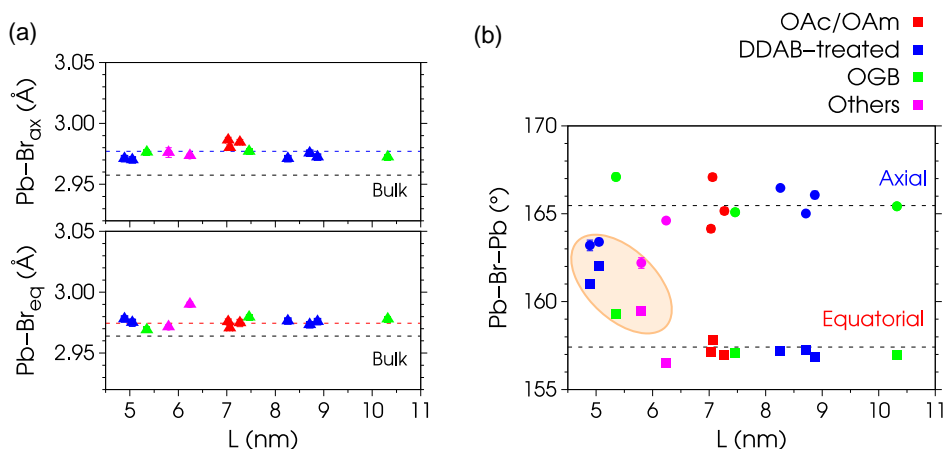
Figure 7. Size effects on the structural parameters of CsPbBr$_3$ NCs (at room temperature). a) Pb—Br$_{eq}$ (average of d_1 and d_2 in Figure 5d) and Pb—Br$_{ax}$ bond distances vs NC size L. Black dashed lines are the corresponding distances in the bulk (ref. [92]), blue and red dashed lines are the distances averaged over all samples. b) Pb—Br$_{eq}$—Pb (squares) and Pb—Br$_{ax}$—Pb (circles) bond angles vs NC size L. Vertical bars in panels (a) and (b), smaller than symbols in most cases, are the uncertainties (details of calculations are available in Supporting Information). The larger spreading of axial angles about the bulk value in 7b reflects the less accurate determination of Br$_{ax}$ position.

to it, and concurrent increase of the lattice distortion in terms of deviation from the cubic one. Moreover, the T-dependence of the lattice anisotropy is different at the intermediate and small NC sizes (and different from the bulk). These findings may contribute to the current debate on the fast emission from bright triplet exciton states in the weak-to-intermediate confinement regime, recently measured also in strongly confined DDAB-capped 5 nm NCs,[36] and on the role of size-dependent structural properties in the dark-bright order of energy levels at room and cryogenic temperatures. In the next paragraph we further analyse the structural changes brought about by cooling down to 6 K, based on WAXTS data measured on 5 nm and 9 nm NCs.

2.5. Static versus Dynamic Disorder in CsPbBr$_3$ NCs

X-ray data collected on dry CsPbBr$_3$ NCs at variable T from 300 K down to 6 K are shown in **Figure 8**a for the 5 nm size and in Figure 8b for the 9 nm size. Inspection of WAXTS patterns suggests that both samples do not undergo any phase transition upon temperature decrease. The superstructure peaks in the 1.5–2.0 Å^{-1} Q-range (the key signatures of the orthorhombic polymorph) are nearly absent in the smallest NCs and do not significantly change their intensity over the probed T-range. In contrast, the 9 nm NCs exhibit progressive fading of 111 peak (in cubic notation, see the central down-arrow in Figure 8b) and the concurrent rise of the two neighbouring peaks (up-arrows).

This behaviour speaks for the progressive narrowing of both the equatorial and axial bending (opposite to the differential profiles shown in Figure 6a), in line with values extracted by WAXTS analyses (details in the Supporting Information) and plotted vs T in Figure 8c (top panel) (values in Table S5 and S6, Supporting Information, best fit in Figure S8, Supporting Information). In terms of PL behaviour, this progressive increase of octahedral tilts upon cooling (inducing a blue shift) slightly counterbalances the dominating and opposite effect of lattice contraction,

resulting in a net (20–10 meV) redshift, as previously reported.[63,86,113,114]

Remarkably, the refined DW factors shown in Figure 8c (bottom panel) indicate a gradual lowering for Br$_{eq}$ and Pb down to quite reasonable values ($\approx$0.8 Å^2) at cryogenic T. In contrast, Br$_{ax}$ shows higher values than Br$_{eq}$ at 300/250 K and anomalously high ($\geq$2.0 Å^2) displacement parameters at lower T down to 6 K. Similar values are reported also for the bulk material studied by neutron powder diffraction down to 4 K.[102] Values of Cs (not shown in Figure 8c, see Table S8, Supporting Information) decrease from 4.5 Å^2 to 1.7 Å^2.

The adoption of isotropic rather than anisotropic displacement parameters[92] does not justify the too high Br$_{ax}$ values obtained at cryogenic T. Indeed, it can be proved that introducing anisotropic (harmonic or non-harmonic) atomic displacement parameters in the DSE (a formidable task per se) would very marginally change the simulated diffraction pattern, well below the noise level they possess. Additional tests, discussed in Figure S9, Supporting Information, dismiss any significant influence of correlation issues of the bromine position on the high values and peculiar T-dependence of DW's shown in Figure 8d.

Besides thermal motions, it is well-known that the atomic displacement parameter may further encode static disorder in diffraction analysis. In such a case, temperature-dependent DW factors described by a monotonically increasing DW(T) function end up with a large-enough DW(0) intercept (well beyond zero-point motions), determined by the atoms residing in closely spaced, but different, minima of the potential energy surface, as observed for Br$_{ax}$ in Figure 8c. Accordingly, we infer that the high remnant DW value for Br$_{ax}$ at low T is due to statically disordered positions and, therefore, disordered octahedral tilts likely accompanied by less extended atomic motions, with possibly coexisting static and dynamic disorder at higher T.[63] That, upon increasing T, dynamic hopping between different minima may occur, lowering the residence lifetime to the ps regime, is more than probable, as suggested in many theoretical
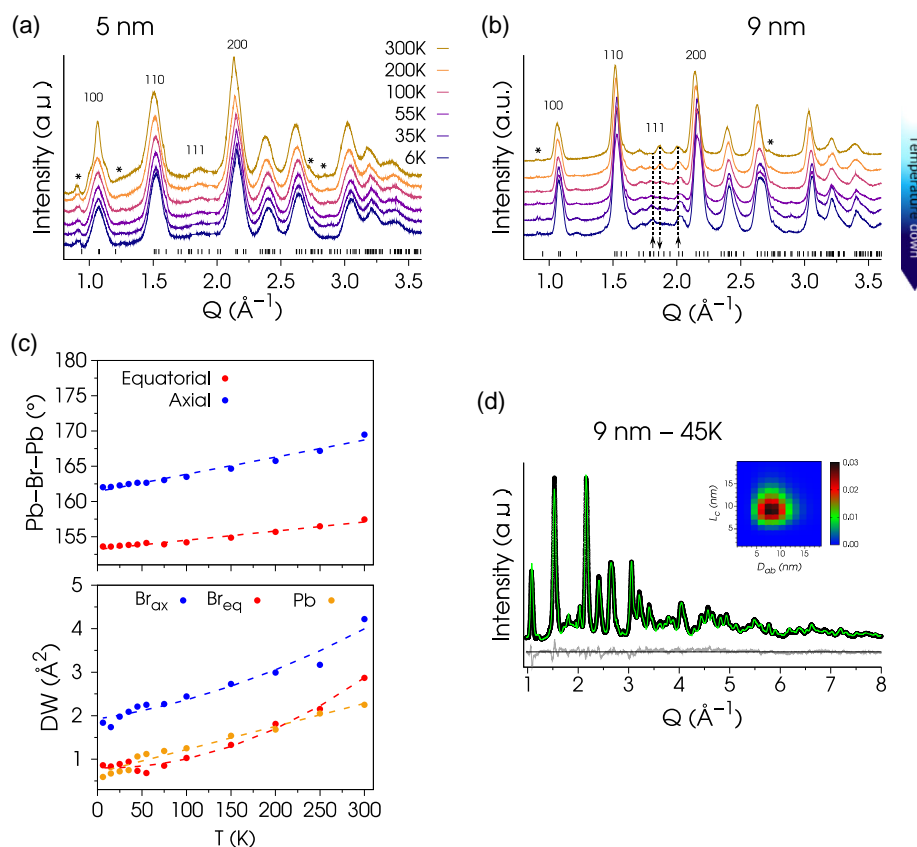
Figure 8. Static and dynamic disorder in dried CsPbBr$_3$ NCs. a) Variable-temperature WAXTS data collected on 5 nm NCs and b) on 9 nm NCs, from 300 K down to 6 K. Asterisks indicate the presence of an impurity in the dried film (Cs$_4$PbBr$_6$, peaks removed from the plot in the 1.6–2.2 Å^{-1} range for sake of clarity), quantified (by Rietveld analysis) to lie in the 2–4 w% range, not affecting the overall conclusions; such an impurity was absent for the colloids studied at room temperature. Up and down arrows in panel (b) highlight intensity changes of superstructure peaks due to the narrowing of both equatorial and axial bending. c) For the 9 nm NCs, the gradual narrowing of equatorial (red dots) and axial (blue dots) bending upon T lowering (top) and the parallel decrease of DW displacement parameters (bottom) for Pb and Br$_{eq}$, whereas Br$_{ax}$ maintains anomalously high values at cryogenic T, revealing a static positional disorder leading to disordered octahedra tilts. Dashed curves are a guide for the eyes. DSE-WAXTS best fit of data at 45 K for the 9 nm NCs d): experimental data (black dots), calculated patterns (green), residual traces (grey). Insets: 2D maps of the bivariate log-normal size distribution.

papers.[63,105,115,116] In this regard, a dedicated modelling is necessary to extract a quantitative and better defined picture of the Br$_{ax}$ static disorder and of its T-dependent evolution. Moreover, the geometrical coherence in the coordination sphere of Pb atoms implies that also Br$_{eq}$ could be involved, to a minor extent, in partial octahedral reorientation.

The behaviour of the 5 nm NCs regarding the Br$_{ax}$ is difficult to extract by Rietveld analysis and requires future work based on accurate grid-search maps. However, the narrowing of equatorial bromine atoms bending and the progressive lowering of DW's of all atoms but Br$_{ax}$ is confirmed (not shown here), despite no clear evidence of changes in the superstructure peak region is visible. We attribute such substantial invariability in that Q-region to the occurrence of a high density of planar defects of the twin boundary type, capable to kill the intensity of superstructure peaks according to the model presented in ref. [74]. Twin boundaries are also detected and modelled in the colloidal sample of the present work (Figure 2b).[36] However, the other small NCs (prepared with ligands different from DDAB) do not show such high

density of defects, suggesting that this feature may not be due to size effects only.

3. Conclusion

In summary, we measured the size-dependent lattice and structural changes in colloidal CsPbBr$_3$ NCs via wide angle X-ray total scattering analysis and atomic-precise modelling in reciprocal space. The intrinsic softness of LHP introduces meaningful lattice and structural response with both size- and T-dependence. On one side, upon downsizing at room temperature, lattice expansion couples to a progressive increase of the orthorhombic strain. On the other side, the T-dependence of the lattice distortion is dissimilar at intermediate and small sizes. These findings may have implications on the bright exciton fine structure emission of strongly confined NCs and contribute to clarify the current debate on the topic. By considering the structural inequivalence of equatorial and axial bromines in the orthorhombic structure, we quantify variations vs the bulk both in Pb–Br

bond distances and in Pb—Br—Pb bond angles. Slightly elongated bond distances (within ≈1% of the bulk) do not show any clear size dependence, whereas at the smallest sizes lattice expansion drives measurable changes of octahedral tilts resulting in equatorial and axial angles of nearly comparable extent (in the bulk they differ by ≈8°). This finding may reconcile (at least partially) the current debate on the role of small sizes in room-temperature stabilization of the cubic crystal polymorph (thermodynamically stable at high temperature), despite that NCs preserve the orthorhombic structure.

Through variable-temperature X-ray experiments performed down to 6 K, we extract a size-independent volumetric thermal expansion coefficient very close to the bulk value, while both equatorial and axial bending narrows upon cooling. We found anomalously high values of the atomic displacement parameter of the axial bromine atom below 200 K, suggesting the presence of statically disordered octahedral tilts, likely coexisting with dynamical disorder at higher T. Future work is encouraged to also extract a clear atomistic model of such static disorder and its implications on the emission properties. Overall, our findings expand the fundamental knowledge on halide perovskite QDs and point to the importance of advancing powerful, atomic-precise methods of analysis in structure–property correlation studies.

We further foresee potential impact of our results on three major aspects of interest in the broad spectrum of applications of LHP QDs: 1) expanding the predictive capability of semiempirical sizing functions, by accounting for structural distortions of ultrasmall NCs as an additional distinct contribution to the optical band gap; 2) considering lattice strain anisotropy of LHP QDs upon cooling as a size-dependent response. This is indeed important for correctly interpreting the excitonic band structure so important for LHP QDs application as quantum source and in quantum information science; 3) providing new knowledge regarding the dynamic/static nature of disorder in LHP, so important for many applications.

4. Experimental Section

Sample Preparation: All samples were prepared according to synthetic procedures previously reported and optimized for the selected sizes.[5] Based on the synthetic approach and type of surface ligands, eleven samples were grouped in three subsets, as follows: oleic acid/oleylammonium (OAc/OAm) (three samples); didodecyldimethyl ammonium bromide (DDAB) (five samples); Oleylguanidinium bromide (OGB) (three samples). The fourth group, labelled as "others", includes three additional sizes, each obtained from a different preparation. Details of the synthesis for each group are available in Section SI, Supporting Information.

Absorbance Measurements: UV–Vis absorption spectra were collected using a Jasco V770 spectrometer operated in transmission mode. Experimental data of optical band gap (1st exciton peak) vs NC size are shown in Figure 1c and fitted using the semi-empirical function provided in Equation (1) and formally derived in ref. [85]. The function provides a general expression predicting the sizing curve of colloidal QDs for many semiconductors (groups III–V, II–VI, IV, IV–VI, and metal halide perovskites), based on known bulk semiconductor parameters

$$E_1(d) = \frac{1}{2}\left[E_0 + \sqrt{E_0^2 + 8|E_0|\alpha\pi^2 \frac{R_\gamma a_0}{\varepsilon_\infty d_0} \frac{e^{-d/d_0}}{(1-e^{-d/d_0})^2}}\right] \quad (1)$$

Where $E_1(d)$ is the size-dependent optical band gap of QDs at the size d (expressed as the diameter of spherical particles), E_0 is the bulk optical band gap, R_γ the Rydberg energy (13.606 eV), a_0 the Bohr radius of hydrogen, ε_∞ the (high frequency) dielectric constant, d_0 the Bohr diameter and $\alpha = 0.7$ an empirical parameter compensating for approximations in the calibration procedure. For cuboidal CsPbBr$_3$ QDs, the function is adapted to account for the impact of the NCs shape on the confinement energy, leading to the edge length L replaced by an equivalent sphere diameter $D_{eq} = 2L/\sqrt{3}$. The predicted size dependence (red dashed curve in Figure 1c) is obtained by using the following values of bulk parameters: $E_0 = 2.38$ eV,[86] $d_0 = 6.1$ nm, $\varepsilon_\infty = 7.3$.[87] The fitted dependence (black dashed curve in Figure 1c) is obtained by relaxing $d_0 = 5.05(8)$ nm.

Photoluminescence (PL) Measurements: A Fluoromax 4 Horiba Jobin Yvon spectrofluorimeter equipped with a PMT detector was used to acquire steady-state PL spectra from solutions. The excitation wavelength was 400 nm, provided by a 150 W xenon lamp dispersed with a monochromator. Measured intensities were corrected for the spectral response of the detector.

Transmission Electron Microscopy: TEM and STEM images were collected using a JEOL JEM-2200FS microscope operated at 200 kV. Abs and PL spectra and TEM images are displayed in Figure S1, Supporting Information.

Synchrotron WAXTS Experiments: WAXTS measurements on CsPbBr$_3$ NCs were performed at the X04SA-MS beamline[117] of the Swiss Light Source (Paul Scherrer Institute, Villigen, CH). Colloidal suspensions (in toluene, hexane, and mesitylene) were loaded in certified glass capillaries (Hilgenberg GmbH G50). For variable-temperature experiments, dry samples were prepared by directly evaporating the solvent inside the capillaries. The photon beam energy was set at 22 keV and the wavelength precisely determined (0.564560 Å) using the NIST 640 d Si powder standard [$a_0 = 5.43123(8)$ Å at 22.5 °C]. Data were collected in the 0.5°–130° 2θ range using a single-photon counting silicon microstrip detector (MYTHEN II).[118] Variable-temperature experiments were performed in the 6–300 K range by using an in-house built He cryostat. T-steps and the sample equilibration at different T values lasted 30 min. Details of the data reduction procedure (capillary/air scattering subtraction and absorption corrections) can be found in Section SII, Supporting Information.

DSE Modelling of WAXTS Data: The DSE-based simulations and data analyses in the present work were performed using the *DebUsSy* suite of programs,[119] relying on a two-step approach. Gaussian sampled interatomic distances[120] and related pseudo-multiplicities are calculated in the first step from the atomistic models of NCs and encoded in suitable databases. The DSE equation[80] is computed in the second step, fed by the set of interatomic distances of a population of NCs. The resulting calculated patterns together with the solvent trace (or additional components, such as Cs$_4$PbBr$_6$ traces for the T-dependent datasets) are linearly combined and scaled to the experimental pattern, and the model structural and microstructural parameters are suitably optimized. Details about the construction of the atomistic models of colloidal and dry CsPbBr$_3$ NCs can be found in the Section SIII, Supporting Information. After a preliminary optimization using a Rietveld approach, a grid search procedure was combined with the *DebUsSy* strategy to precisely determine the coordinates of the two crystallographically independent bromines (Br$_{eq}$ and Br$_{ax}$) within the *Pbnm* crystal structure of all CsPbBr$_3$ samples analysed. Through this approach, we modified the *x, y, z* fractional coordinates of Br$_{eq}$ and *x, y* of Br$_{ax}$ (being *z* fixed at 0.75, as dictated by the *Pbnm* space group symmetry, with Pb in 0,0,0.5) and the *DW* parameters for both atoms. For each grid point, the goodness of fit [GoF = $(\chi^2)^{1/2}$] was computed to quantitatively determine the match between the experimental data and the DSE model. More details about this procedure can be found in Section SIV, Supporting Information. Numerical outcomes of the structural and microstructural characterization of all investigated CsPbBr$_3$ samples at room temperature, and for the 5 nm and 9 nm DDAB-capped NCs in the 6–300 K T-range are synoptically collected in the Figure S2–S9 and Table S2–S8, Supporting Information.

**ADVANCED
SCIENCE NEWS**

www.advancedsciencenews.com

**small
structures**

www.small-structures.com

Supporting Information

Acknowledgements

Conflict of Interest

The authors declare no conflict of interest.

Data Availability Statement

The data that support the findings of this study are available from the corresponding author upon reasonable request.

Keywords

[1] M. V. Kovalenko, L. Protesescu, M. I. Bodnarchuk, *Science* **2017**, *358*, 745.

[2] A. Dey, J. Ye, A. De, E. Debroye, S. K. Ha, E. Bladt, A. S. Kshirsagar, Z. Wang, J. Yin, Y. Wang, L. N. Quan, F. Yan, M. Gao, X. Li, J. Shamsi, T. Debnath, M. Cao, M. A. Scheel, S. Kumar, J. A. Steele, M. Gerhard, L. Chouhan, K. Xu, X. Wu, Y. Li, Y. Zhang, A. Dutta, C. Han, I. Vincon, A. L. Rogach, et al., *ACS Nano* **2021**, *15*, 10775.

[3] H. Huang, M. I. Bodnarchuk, S. V. Kershaw, M. V. Kovalenko, A. L. Rogach, *ACS Energy Lett.* **2017**, *2*, 2071.

[4] Q. A. Akkerman, G. Rainò, M. V. Kovalenko, L. Manna, *Nat. Mater.* **2018**, *17*, 394.

[5] L. Protesescu, S. Yakunin, M. I. Bodnarchuk, F. Krieg, R. Caputo, C. H. Hendon, R. X. Yang, A. Walsh, M. V. Kovalenko, *Nano Lett.* **2015**, *15*, 3692.

[6] Q. Lin, Y. Zhu, Y. Wang, D. Li, Y. Zhao, Y. Liu, F. Li, W. Huang, *Adv. Mater.* **2023**, *35*, 2210385.

[7] J. Kim, J. Roh, M. Park, C. Lee, *Adv. Mater.* **2023**, 2212220.

[8] H. Utzat, W. Sun, A. E. K. Kaplan, F. Krieg, M. Ginterseder, B. Spokoyny, N. D. Klein, K. E. Shulenberger, C. F. Perkinson, M. V. Kovalenko, M. G. Bawendi, *Science* **2019**, *363*, 1068.

[9] C. Zhu, M. Marczak, L. Feld, S. C. Boehme, C. Bernasconi, A. Moskalenko, I. Cherniukh, D. Dirin, M. I. Bodnarchuk, M. V. Kovalenko, G. Rainò, *Nano Lett.* **2022**, *22*, 3751.

[10] D. Jia, J. Chen, R. Zhuang, Y. Hua, X. Zhang, *Adv. Mater.* **2023**, *35*, 2212160.

[11] B. M. Wieliczka, S. N. Habisreutinger, K. Schutt, J. L. Blackburn, J. M. Luther, *Adv. Energy Mater.* **2023**, *13*, 2204351.

[12] M. Hao, Y. Bai, S. Zeiske, L. Ren, J. Liu, Y. Yuan, N. Zarrabi, N. Cheng, M. Ghasemi, P. Chen, M. Lyu, D. He, J.-H. Yun, Y. Du, Y. Wang, S. Ding, A. Armin, P. Meredith, G. Liu, H.-M. Cheng, L. Wang, *Nat. Energy* **2020**, *5*, 79.

[13] J. Song, J. Li, X. Li, L. Xu, Y. Dong, H. Zeng, *Adv. Mater.* **2015**, *27*, 7162.

[14] E. M. Sanehira, A. R. Marshall, J. A. Christians, S. P. Harvey, P. N. Ciesielski, L. M. Wheeler, P. Schulz, L. Y. Lin, M. C. Beard, J. M. Luther, *Sci. Adv.* **2017**, *3*, eaao4204.

[15] T. Chiba, K. Hoshi, Y.-J. Pu, Y. Takeda, Y. Hayashi, S. Ohisa, S. Kawata, J. Kido, *ACS Appl. Mater. Interfaces* **2017**, *9*, 18054.

[16] M. Ma, X. Zhang, L. Xu, X. Chen, L. Wang, T. Cheng, F. Wei, J. Yuan, B. Shen, *Adv. Mater.* **2023**, *35*, 2300653.

[17] Q. A. Akkerman, T. P. T. Nguyen, S. C. Boehme, F. Montanarella, D. N. Dirin, P. Wechsler, F. Beiglböck, G. Rainò, R. Erni, C. Katan, J. Even, M. V. Kovalenko, *Science* **2022**, *377*, 1406.

[18] Y. Shynkarenko, M. I. Bodnarchuk, C. Bernasconi, Y. Berezovska, V. Verteletskyi, S. T. Ochsenbein, M. V. Kovalenko, *ACS Energy Lett.* **2019**, *4*, 2703.

[19] M. I. Bodnarchuk, S. C. Boehme, S. ten Brinck, C. Bernasconi, Y. Shynkarenko, F. Krieg, R. Widmer, B. Aeschlimann, D. Günther, M. V. Kovalenko, I. Infante, *ACS Energy Lett.* **2019**, *4*, 63.

[20] A. Garai, R. K. Behera, N. Pradhan, *J. Phys. Chem. C* **2022**, *126*, 16759.

[21] S. ten Brinck, F. Zaccaria, I. Infante, *ACS Energy Lett.* **2019**, *4*, 2739.

[22] N. Fiuza-Maneiro, K. Sun, I. López-Fernández, S. Gómez-Graña, P. Müller-Buschbaum, L. Polavarapu, *ACS Energy Lett.* **2023**, *8*, 1152.

[23] N. Pradhan, *ACS Phys. Chem. Au* **2022**, *2*, 268.

[24] F. Zaccaria, B. Zhang, L. Goldoni, M. Imran, J. Zito, B. van Beek, S. Lauciello, L. De Trizio, L. Manna, I. Infante, *ACS Nano* **2022**, *16*, 1444.

[25] S. K. Bera, S. Bera, M. Shrivastava, N. Pradhan, K. V. Adarsh, *Nano Lett.* **2022**, *22*, 8908.

[26] P. Ijaz, M. Imran, M. M. Soares, H. C. N. Tolentino, B. Martín-García, C. Giannini, I. Moreels, L. Manna, R. Krahne, *J. Phys. Chem. Lett.* **2020**, *11*, 2079.

[27] J. M. Ball, A. Petrozza, *Nat. Energy* **2016**, *1*, 16149.

[28] S. ten Brinck, I. Infante, *ACS Energy Lett.* **2016**, *1*, 1266.

[29] C. Bi, S. Wang, S. V. Kershaw, K. Zheng, T. Pullerits, S. Gaponenko, J. Tian, A. L. Rogach, *Adv. Sci.* **2019**, *6*, 1900462.

[30] D. D. Blach, V. A. Lumsargis, D. E. Clark, C. Chuang, K. Wang, L. Dou, R. D. Schaller, J. Cao, C. W. Li, L. Huang, *Nano Lett.* **2022**, *22*, 7811.

[31] G. Rainò, M. A. Becker, M. I. Bodnarchuk, R. F. Mahrt, M. V. Kovalenko, T. Stöferle, *Nature* **2018**, *563*, 671.

[32] D. Baranov, S. Toso, M. Imran, L. Manna, *J. Phys. Chem. Lett.* **2019**, *10*, 655.

[33] F. Krieg, P. C. Sercel, M. Burian, H. Andrusiv, M. I. Bodnarchuk, T. Stöferle, R. F. Mahrt, D. Naumenko, H. Amenitsch, G. Rainò, M. V. Kovalenko, *ACS Cent. Sci.* **2021**, *7*, 135.

[34] F. Krieg, Q. K. Ong, M. Burian, G. Rainò, D. Naumenko, H. Amenitsch, A. Süess, M. J. Grotevent, F. Krumeich, M. I. Bodnarchuk, I. Shorubalko, F. Stellacci, M. V. Kovalenko, *J. Am. Chem. Soc.* **2019**, *141*, 19839.

**ADVANCED
SCIENCE NEWS**

www.advancedsciencenews.com

**small
structures**

www.small-structures.com

[35] F. Bertolotti, A. Vivani, F. Ferri, P. Anzini, A. Cervellino, M. I. Bodnarchuk, G. Nedelcu, C. Bernasconi, M. V. Kovalenko, N. Masciocchi, A. Guagliardi, *Chem. Mater.* **2022**, *34*, 594.

[36] S. C. Boehme, M. I. Bodnarchuk, M. Burian, F. Bertolotti, I. Cherniukh, C. Bernasconi, C. Zhu, R. Erni, H. Amenitsch, D. Naumenko, H. Andrusiv, N. Semkiv, R. A. John, A. Baldwin, K. Galkowski, N. Masciocchi, S. D. Stranks, G. Rainò, A. Guagliardi, M. V. Kovalenko, *ACS Nano* **2023**, *17*, 2089.

[37] Y. Lv, C. Yin, C. Zhang, W. W. Yu, X. Wang, Y. Zhang, M. Xiao, *Nano Lett.* **2019**, *19*, 4442.

[38] G. Rainò, G. Nedelcu, L. Protesescu, M. I. Bodnarchuk, M. V. Kovalenko, R. F. Mahrt, T. Stöferle, *ACS Nano* **2016**, *10*, 2485.

[39] P. Tamarat, L. Hou, J.-B. Trebbia, A. Swarnkar, L. Biadala, Y. Louyer, M. I. Bodnarchuk, M. V. Kovalenko, J. Even, B. Lounis, *Nat. Commun.* **2020**, *11*, 6001.

[40] G. Rainò, N. Yazdani, S. C. Boehme, M. Kober-Czerny, C. Zhu, F. Krieg, M. D. Rossell, R. Erni, V. Wood, I. Infante, M. V. Kovalenko, *Nat. Commun.* **2022**, *13*, 2587.

[41] C. Zhu, T. Nguyen, S. C. Boehme, A. Moskalenko, D. N. Dirin, M. I. Bodnarchuk, C. Katan, J. Even, G. Rainò, M. V. Kovalenko, *Adv. Mater.* **2023**, *35*, 2208354.

[42] Q. Zhao, A. Hazarika, L. T. Schelhas, J. Liu, E. A. Gaulding, G. Li, M. Zhang, M. F. Toney, P. C. Sercel, J. M. Luther, *ACS Energy Lett.* **2020**, *5*, 238.

[43] A. A. Koegel, E. M. Mozur, I. W. H. Oswald, N. H. Jalarvo, T. R. Prisk, M. Tyagi, J. R. Neilson, *J. Am. Chem. Soc.* **2022**, *144*, 1313.

[44] J.-K. Chen, Q. Zhao, N. Shirahata, J. Yin, O. M. Bakr, O. F. Mohammed, H.-T. Sun, *ACS Mater. Lett.* **2021**, *3*, 845.

[45] J. A. Steele, V. Prakasam, H. Huang, E. Solano, D. Chernyshov, J. Hofkens, M. B. J. Roeffaers, *J. Am. Chem. Soc.* **2021**, *143*, 10500.

[46] Y. Ha, J.-G. Park, K.-H. Hong, H. Kim, *J. Am. Chem. Soc.* **2022**, *144*, 297.

[47] I. Levchuk, A. Osvet, X. Tang, M. Brandl, J. D. Perea, F. Hoegl, G. J. Matt, R. Hock, M. Batentschuk, C. J. Brabec, *Nano Lett.* **2017**, *17*, 2765.

[48] L. Protesescu, S. Yakunin, S. Kumar, J. Bar, F. Bertolotti, N. Masciocchi, A. Guagliardi, M. Grotevent, I. Shorubalko, M. I. Bodnarchuk, C. J. Shih, M. V. Kovalenko, *ACS Nano* **2017**, *11*, 3119.

[49] I. Lignos, V. Morad, Y. Shynkarenko, C. Bernasconi, R. M. Maceiczyk, L. Protesescu, F. Bertolotti, S. Kumar, S. T. Ochsenbein, N. Masciocchi, A. Guagliardi, C.-J. Shih, M. I. Bodnarchuk, A. J. deMello, M. V. Kovalenko, *ACS Nano* **2018**, *12*, 5504.

[50] G. E. Eperon, D. S. Ginger, *ACS Energy Lett.* **2017**, *2*, 1190.

[51] T. A. de Souza Carvalho, L. F. Magalhaes, C. I. do Livramento Santos, T. A. Z. de Freitas, B. R. Carvalho Vale, A. F. Vale da Fonseca, M. A. Schiavon, *Chem. Eur. J.* **2023**, *29*, e202202518.

[52] K. Sandeep, K. Padmakumar, K. U. Ambili, P. Jishnu, K. H. Fousia, A. R. Ramesh, J. P. Rappai, V. Santhi, M. Shanthil, *Phys. Status Solidi B* **2022**, *259*, 2100600.

[53] G. Nedelcu, L. Protesescu, S. Yakunin, M. I. Bodnarchuk, M. J. Grotevent, M. V. Kovalenko, *Nano Lett.* **2015**, *15*, 5635.

[54] E. Scharf, F. Krieg, O. Elimelech, M. Oded, A. Levi, D. N. Dirin, M. V. Kovalenko, U. Banin, *Nano Lett.* **2022**, *22*, 4340.

[55] A. Ummadisingu, S. Meloni, A. Mattoni, W. Tress, M. Grätzel, *Angew. Chem., Int. Ed. Engl.* **2021**, *60*, 21368.

[56] R. Prasanna, A. Gold-Parker, T. Leijtens, B. Conings, A. Babayigit, H.-G. Boyen, M. F. Toney, M. D. McGehee, *J. Am. Chem. Soc.* **2017**, *139*, 11117.

[57] S. M. Lee, C. J. Moon, H. Lim, Y. Lee, M. Y. Choi, J. Bang, *J. Phys. Chem. C* **2017**, *121*, 26054.

[58] M. A. Becker, R. Vaxenburg, G. Nedelcu, P. C. Sercel, A. Shabaev, M. J. Mehl, J. G. Michopoulos, S. G. Lambrakos, N. Bernstein, J. L. Lyons, T. Stoferle, R. F. Mahrt, M. V. Kovalenko, D. J. Norris, G. Raino, A. L. Efros, *Nature* **2018**, *553*, 189.

[59] P. C. Sercel, J. L. Lyons, D. Wickramaratne, R. Vaxenburg, N. Bernstein, A. L. Efros, *Nano Lett.* **2019**, *19*, 4068.

[60] Y. Han, W. Liang, X. Lin, Y. Li, F. Sun, F. Zhang, P. C. Sercel, K. Wu, *Nat. Mater.* **2022**, *21*, 1282.

[61] M.-R. Amara, Z. Said, C. Huo, A. Pierret, C. Voisin, W. Gao, Q. Xiong, C. Diederichs, *Nano Lett.* **2023**, *23*, 3607.

[62] P. C. Sercel, J. L. Lyons, N. Bernstein, A. L. Efros, *J. Chem. Phys.* **2019**, *151*, 234106.

[63] O. Cannelli, J. Wiktor, N. Colonna, L. Leroy, M. Puppin, C. Bacellar, I. Sadykov, F. Krieg, G. Smolentsev, M. V. Kovalenko, A. Pasquarello, M. Chergui, G. F. Mancini, *J. Phys. Chem. Lett.* **2022**, *13*, 3382.

[64] O. Cannelli, N. Colonna, M. Puppin, T. C. Rossi, D. Kinschel, L. M. D. Leroy, J. Löffler, J. M. Budarz, A. M. March, G. Doumy, A. Al Haddad, M.-F. Tu, Y. Kumagai, D. Walko, G. Smolentsev, F. Krieg, S. C. Boehme, M. V. Kovalenko, M. Chergui, G. F. Mancini, *J. Am. Chem. Soc.* **2021**, *143*, 9048.

[65] N. Yazdani, M. I. Bodnarchuk, F. Bertolotti, N. Masciocchi, I. Fureraj, B. Guzelturk, B. L. Cotts, M. Zajac, G. Rainò, M. Jansen, S. C. Boehme, M. Yarema, M.-F. Lin, M. Kozina, A. Reid, X. Shen, S. Weathersby, X. Wang, E. Vauthey, A. Guagliardi, M. V. Kovalenko, V. Wood, A. Lindenberg, *Nat. Phys.* **2023**, https://doi.org/10.1038/s41567-023-02253-7.

[66] T. Lanigan-Atkins, X. He, M. J. Krogstad, D. M. Pajerowski, D. L. Abernathy, G. N. M. N. Xu, Z. Xu, D.-Y. Chung, M. G. Kanatzidis, S. Rosenkranz, R. Osborn, O. Delaire, *Nat. Mater.* **2021**, *20*, 977.

[67] M. C. Brennan, M. Kuno, S. Rouvimov, *Inorg. Chem.* **2019**, *58*, 1555.

[68] C. Wang, A. S. R. Chesman, J. J. Jasieniak, *Chem. Commun.* **2016**, *53*, 232.

[69] F. Liu, Y. Zhang, C. Ding, S. Kobayashi, T. Izuishi, N. Nakazawa, T. Toyoda, T. Ohta, S. Hayase, T. Minemoto, K. Yoshino, S. Dai, Q. Shen, *ACS Nano* **2017**, *11*, 10373.

[70] C. Liu, Y. Yang, X. Liu, Y. Ding, Z. Arain, X. Li, Y. Li, Z. Zhou, S. Dai, M. K. Nazeeruddin, *J. Mater. Chem. A* **2020**, *8*, 10226.

[71] A. Swarnkar, A. R. Marshall, E. M. Sanehira, B. D. Chernomordik, D. T. Moore, J. A. Christians, T. Chakrabarti, J. M. Luther, *Science* **2016**, *354*, 92.

[72] G. Laurita, D. H. Fabini, C. C. Stoumpos, M. G. Kanatzidis, R. Seshadri, *Chem. Sci.* **2017**, *8*, 5628.

[73] L. Gao, L. Yadgarov, R. Sharma, R. Korobko, K. M. McCall, D. H. Fabini, C. C. Stoumpos, M. G. Kanatzidis, A. M. Rappe, O. Yaffe, *Mater. Adv.* **2021**, *2*, 4610.

[74] F. Bertolotti, L. Protesescu, M. V. Kovalenko, S. Yakunin, A. Cervellino, S. J. L. Billinge, M. W. Terban, J. S. Pedersen, N. Masciocchi, A. Guagliardi, *ACS Nano* **2017**, *11*, 3819.

[75] K. Wang, G. Xing, Q. Song, S. Xiao, *Adv. Mater.* **2021**, *33*, 2000306.

[76] Y. Fu, H. Zhu, J. Chen, M. P. Hautzinger, X.-Y. Zhu, S. Jin, *Nat. Rev. Mater.* **2019**, *4*, 169.

[77] K. Chen, S. Schünemann, S. Song, H. Tüysüz, *Chem. Soc. Rev.* **2018**, *47*, 7045.

[78] F. Bertolotti, D. Moscheni, A. Guagliardi, N. Masciocchi, *Eur. J. Inorg. Chem.* **2018**, *2018*, 3789.

[79] A. Cervellino, R. Frison, N. Masciocchi, A. Guagliardi, in (Ed: C. S. S. R. Kumar), *CRC Concise Encyclopedia of Nanotechnology*, Springer-Verlag GmbH Germany, Berlin, Germany **2016**, pp. 545–608.

[80] P. Debye, *Ann. Phys.* **1915**, *351*, 809.

[81] D. Moscheni, F. Bertolotti, L. Piveteau, L. Protesescu, D. N. Dirin, M. V. Kovalenko, A. Cervellino, J. S. Pedersen, N. Masciocchi, A. Guagliardi, *ACS Nano* **2018**, *12*, 12558.

[82] F. Bertolotti, D. N. Dirin, M. Ibanez, F. Krumeich, A. Cervellino, R. Frison, O. Voznyy, E. H. Sargent, M. V. Kovalenko, A. Guagliardi, N. Masciocchi, *Nat. Mater.* **2016**, *15*, 987.

[83] L. Protesescu, S. Yakunin, M. I. Bodnarchuk, F. Bertolotti, N. Masciocchi, A. Guagliardi, M. V. Kovalenko, *J. Am. Chem. Soc.* **2016**, *138*, 14202.

[84] D. N. Dirin, A. Vivani, M. Zacharias, T. V. Sekh, I. Cherniukh, S. Yakunin, F. Bertolotti, M. Aebli, R. D. Schaller, A. Wieczorek, S. Siol, C. Cancellieri, L. P. H. Jeurgens, N. Masciocchi, A. Guagliardi, L. Pedesseau, J. Even, M. V. Kovalenko, M. I. Bodnarchuk, *Nano Lett.* **2023**, *23*, 1914.

[85] T. Aubert, A. A. Golovatenko, M. Samoli, L. Lermusiaux, T. Zinn, B. Abécassis, A. V. Rodina, Z. Hens, *Nano Lett.* **2022**, *22*, 1778.

[86] G. Mannino, I. Deretzis, E. Smecca, A. La Magna, A. Alberti, D. Ceratti, D. Cahen, *J. Phys. Chem. Lett.* **2020**, *11*, 2490.

[87] Z. Yang, A. Surrente, K. Galkowski, A. Miyata, O. Portugall, R. J. Sutton, A. A. Haghighirad, H. J. Snaith, D. K. Maude, P. Plochocka, R. J. Nicholas, *ACS Energy Lett.* **2017**, *2*, 1621.

[88] J. Maes, N. Castro, K. De Nolf, W. Walravens, B. Abécassis, Z. Hens, *Chem. Mater.* **2018**, *30*, 3952.

[89] P. Cottingham, R. L. Brutchey, *Chem. Commun.* **2016**, *52*, 5246.

[90] F. Bertolotti, G. Nedelcu, A. Vivani, A. Cervellino, N. Masciocchi, A. Guagliardi, M. V. Kovalenko, *ACS Nano* **2019**, *13*, 14294.

[91] G. Cernuto, N. Masciocchi, A. Cervellino, G. M. Colonna, A. Guagliardi, *J. Am. Chem. Soc.* **2011**, *133*, 3114.

[92] C. C. Stoumpos, C. D. Malliakas, J. A. Peters, Z. Liu, M. Sebastian, J. Im, T. C. Chasapis, A. C. Wibowo, D. Y. Chung, A. J. Freeman, B. W. Wessels, M. G. Kanatzidis, *Cryst. Growth Des.* **2013**, *13*, 2722.

[93] P. Cottingham, R. L. Brutchey, *Chem. Mater.* **2016**, *28*, 7574.

[94] X.-G. Zhao, G. M. Dalpian, Z. Wang, A. Zunger, *Phys. Rev. B* **2020**, *101*, 155137.

[95] T. A. S. Doherty, S. Nagane, D. J. Kubicki, Y.-K. Jung, D. N. Johnstone, A. N. Iqbal, D. Guo, K. Frohna, M. Danaie, E. M. Tennyson, S. Macpherson, A. Abfalterer, M. Anaya, Y.-H. Chiang, P. Crout, F. S. Ruggeri, S. Collins, C. P. Grey, A. Walsh, P. A. Midgley, S. D. Stranks, *Science* **2021**, *374*, 1598.

[96] F. C. Hanusch, E. Wiesenmayer, E. Mankel, A. Binek, P. Angloher, C. Fraunhofer, N. Giesbrecht, J. M. Feckl, W. Jaegermann, D. Johrendt, T. Bein, P. Docampo, *J. Phys. Chem. Lett.* **2014**, *5*, 2791.

[97] V. B. Mykhaylyk, H. Kraus, V. Kapustianyk, H. J. Kim, P. Mercere, M. Rudko, P. Da Silva, O. Antonyak, M. Dendebera, *Sci. Rep.* **2020**, *10*, 8601.

[98] P. Tamarat, E. Prin, Y. Berezovska, A. Moskalenko, T. P. T. Nguyen, C. Xia, L. Hou, J.-B. Trebbia, M. Zacharias, L. Pedesseau, C. Katan, M. I. Bodnarchuk, M. V. Kovalenko, J. Even, B. Lounis, *Nat. Commun.* **2023**, *14*, 229.

[99] E. Kirstein, D. S. Smirnov, E. A. Zhukov, D. R. Yakovlev, N. E. Kopteva, D. N. Dirin, O. Hordiichuk, M. V. Kovalenko, M. Bayer, *Nat. Commun.* **2023**, *14*, 6683.

[100] C. Bujalance, L. Calio, D. N. Dirin, D. O. Tiede, J. F. Galisteo-Lopez, J. Feist, F. J. Garcia-Vidal, M. V. Kovalenko, H. Miguez, arXiv:2306.10884 [cond-mat.mtrl-sci], **2023**.

[101] A. Bornschlegl, M. Lichtenegger, L. Luber, C. Lampe, M. Bodnarchuk, M. V. Kovalenko, A. Urban, PREPRINT (Version 1) available at Research Square **2023**, https://doi.org/10.21203/rs.3.rs-2450378/v1.

[102] C. A. López, C. Abia, M. C. Alvarez-Galván, B.-K. Hong, M. V. Martínez-Huerta, F. Serrano-Sánchez, F. Carrascoso, A. Castellanos-Gómez, M. T. Fernández-Díaz, J. A. Alonso, *ACS Omega* **2020**, *5*, 5931.

[103] A. M. Glazer, *Acta Crystallogr., Sect. A* **1975**, *31*, 756.

[104] A. Cohen, T. M. Brenner, J. Klarbring, R. Sharma, D. H. Fabini, R. Korobko, P. K. Nayak, O. Hellman, O. Yaffe, *Adv. Mater.* **2022**, *34*, 2107932.

[105] A. Marronnier, H. Lee, B. Geffroy, J. Even, Y. Bonnassieux, G. Roma, *J. Phys. Chem. Lett.* **2017**, *8*, 2659.

[106] J. S. Bechtel, J. C. Thomas, A. Van der Ven, *Phys. Rev. Mater.* **2019**, *3*, 113605.

[107] C. Gehrmann, D. A. Egger, *Nat. Commun.* **2019**, *10*, 3141.

[108] M. Sakata, J. Harada, M. J. Cooper, K. D. Rouse, *Acta Crystallogr., Sect. A* **1980**, *36*, 7.

[109] M. S. Kirschner, B. T. Diroll, P. Guo, S. M. Harvey, W. Helweh, N. C. Flanders, A. Brumberg, N. E. Watkins, A. A. Leonard, A. M. Evans, M. R. Wasielewski, W. R. Dichtel, X. Zhang, L. X. Chen, R. D. Schaller, *Nat. Commun.* **2019**, *10*, 504.

[110] T. Debnath, D. Sarker, H. Huang, Z.-K. Han, A. Dey, L. Polavarapu, S. V. Levchenko, J. Feldmann, *Nat. Commun.* **2021**, *12*, 2629.

[111] X. Wu, L. Z. Tan, X. Shen, T. Hu, K. Miyata, M. T. Trinh, R. Li, R. Coffee, S. Liu, D. A. Egger, I. Makasyuk, Q. Zheng, A. Fry, J. S. Robinson, M. D. Smith, B. Guzelturk, H. I. Karunadasa, X. Wang, X. Zhu, L. Kronik, A. M. Rappe, A. M. Lindenberg, *Sci. Adv.* **2017**, *3*, e1602388.

[112] H. Seiler, D. Zahn, V. C. A. Taylor, M. I. Bodnarchuk, Y. W. Windsor, M. V. Kovalenko, R. Ernstorfer, *ACS Nano* **2023**, *17*, 1979.

[113] B. Ai, C. Liu, Z. Deng, J. Wang, J. Han, X. Zhao, *Phys. Chem. Chem. Phys.* **2017**, *19*, 17349.

[114] K. Wei, Z. Xu, R. Chen, X. Zheng, X. Cheng, T. Jiang, *Opt. Lett.* **2016**, *41*, 3821.

[115] R. X. Yang, J. M. Skelton, E. L. da Silva, J. M. Frost, A. Walsh, *J. Phys. Chem. Lett.* **2017**, *8*, 4720.

[116] X. Zhu, S. Caicedo-Dávila, C. Gehrmann, D. A. Egger, *ACS Appl. Mater. Interfaces* **2022**, *14*, 22973.

[117] P. R. Willmott, D. Meister, S. J. Leake, M. Lange, A. Bergamaschi, M. Böge, M. Calvi, C. Cancellieri, N. Casati, A. Cervellino, Q. Chen, C. David, U. Flechsig, F. Gozzo, B. Henrich, S. Jäggi-Spielmann, B. Jakob, I. Kalichava, P. Karvinen, J. Krempasky, A. Lüdeke, R. Lüscher, S. Maag, C. Quitmann, M. L. Reinle-Schmitt, T. Schmidt, B. Schmitt, A. Streun, I. Vartiainen, M. Vitins, et al., *J. Synchrotron Radiat.* **2013**, *20*, 667.

[118] A. Bergamaschi, A. Cervellino, R. Dinapoli, F. Gozzo, B. Henrich, I. Johnson, P. Kraft, A. Mozzanica, B. Schmitt, X. Shi, *J. Synchrotron Radiat.* **2010**, *17*, 653.

[119] A. Cervellino, R. Frison, F. Bertolotti, A. Guagliardi, *J. Appl. Cryst.* **2015**, *48*, 2026.

[120] A. Cervellino, C. Giannini, A. Guagliardi, *J. Comput. Chem.* **2006**, *27*, 995.